



In Situ Measurement of Radial Temperature Distributions in Cylindrical Li-Ion Cells

Guangsheng Zhang,^{a,*} Lei Cao,^a Shanhai Ge,^{a,*} Chao-Yang Wang,^{a,b,*,z}
Christian E. Shaffer,^b and Christopher D. Rahn^a

^aElectrochemical Engine Center (ECEC), and Department of Mechanical & Nuclear Engineering, The Pennsylvania State University, University Park, Pennsylvania 16802, USA

^bEC Power, State College, Pennsylvania 16803, USA

Temperature is critical to the performance, durability and safety of Li-ion batteries. This paper reports in situ measurement of the radial temperature distribution inside a cylindrical Li-ion battery cell. 18650-size cylindrical cells with multiple micro thermocouples embedded are designed and manufactured. The radial temperature distribution is obtained under various operating conditions. The effects of critical parameters, such as discharge C rate, ambient temperature, and cooling condition, are investigated. It is found that higher discharge C rate and lower ambient temperature lead to higher temperature rise and larger temperature gradient within the battery cell. Stronger cooling results in smaller temperature rise but larger temperature gradient. Correlation between relative temperature gradient and cooling coefficient suggests that the assumption of uniform temperature distribution is applicable under natural-convection conditions but not applicable under strong forced convection conditions. The present results provide valuable experimental data that can be readily used to validate electrochemical-thermal coupled (ECT) battery models.
© 2014 The Electrochemical Society. [DOI: 10.1149/2.0051410jes] All rights reserved.

Manuscript submitted April 30, 2014; revised manuscript received June 16, 2014. Published July 1, 2014.

Driven by the ever-increasing applications in electric vehicles and grand challenges,¹⁻⁴ the need for Li-ion batteries with enhanced performance, durability and safety is increasing. Previous studies show that temperature is critical to the performance, durability and safety of Li-ion batteries.⁵⁻²⁵ On one hand, the performance is reduced at lower temperatures,⁶⁻¹¹ and too low temperature can even cause detrimental lithium plating during charge.¹²⁻¹⁴ On the other hand, a Li-ion battery degrades considerably faster at higher temperatures,¹⁵⁻¹⁹ and excessively high temperature can lead to breakdown of the solid electrolyte interface (SEI) layer,²⁰⁻²² electrolyte decomposition,²³⁻²⁵ and even to disastrous thermal runaway.^{2,26,27}

The surface temperatures of Li-ion cells, batteries and battery packs are commonly monitored.^{28,29} However, surface temperature is expected to be different from internal temperature due to the very low thermal conductivity ($\sim 1 \text{ W m}^{-1} \text{ K}^{-1}$) of electrodes and separator in the through plane direction.^{5,30-32} This spatial temperature distribution inside a Li-ion battery may exacerbate the non-uniform distribution of current density³³⁻³⁵ due to complex interactions among local reaction current, state of charge (SOC) and temperature. Under extreme conditions, e.g. accidental short circuit or overcharge, substantial heat is generated internally and monitoring of surface temperature could significantly underestimate the maximum temperature. Measuring internal temperature can thus provide more accurate information and is a better indicator of the health and safety of a Li-ion battery.

In addition, electrochemical-thermal coupled (ECT) modeling has been widely used in the research and development of Li-ion batteries to gain insight into internal processes, to optimize battery design and operation, as well as to improve performance, durability and safety.^{11,36-43} Experimental internal temperature distribution data can provide a critical source of validation for multi-dimensional ECT models that are increasingly used.⁴⁴⁻⁵⁷ Other ECT models use a lumped capacitance method that assumes uniform temperature distribution inside a Li-ion cell. In situ measurement of temperature distribution can provide valuable benchmark data to examine the validity of the assumption under various conditions.

In situ measurement of internal temperatures in Li-ion cell has received some attention, but reports are still very limited, especially for distributions of multiple local temperatures. Leising et al.^{58,59} measured central and surface temperatures of 1.5 Ah prismatic cells during overcharge and short circuit testing. Zeng et al.⁶⁰ measured central and surface temperatures of a 0.65 Ah prismatic cell during overcharge. Using a specially designed nail with an inserted thermocouple, Hatchard et al.⁶¹ measured local temperature at the site of nail

penetration during nail penetration testing. Significant differences between internal temperature and surface temperature were observed under such abuse conditions.⁵⁸⁻⁶¹ Onda et al.^{62,63} reported measurements of central temperature in 18650-size cylindrical cells and found that the differences from surface temperature were very small. Forgez et al.⁶⁴ inserted a thermocouple with an external diameter of 1 mm into the center of a 26650-size cylindrical cell by drilling to access the central hole of the jelly roll. The temperature measured by the internal thermocouple was very different from the surface temperature during high C rate pulse charge/discharge. They also recorded surface temperatures using infrared thermography, which showed very slight temperature differences at different locations on the surface. Lee et al. developed flexible micro temperature sensors for measurement of internal temperature in Li-ion cells and demonstrated their potential applications in coin cells⁶⁵ and pouch cells.^{66,67} Based on a correlation between internal temperature and phase shift in the impedance of a Li-ion cell within a certain temperature and frequency range, Srinivasan et al.^{68,69} reported a non-intrusive method to predict internal temperature by measuring phase shift. Schmidt et al.⁷⁰ reported a modified version of that method, taking into account the effects of state of charge (SOC). Recently, Li et al.⁷¹ measured temperature distributions in two large format pouch cells with embedded thermocouples. The temperature gradient was found to be significant in the in-plane direction but not significant in the through-plane direction.

Although some interesting results have been reported, as briefly reviewed above, there lacks a systematic understanding about internal temperature distribution under various conditions. There are little experimental data that can be readily used for model validation, especially for spirally wound Li-ion cells. Some studies focus on the development of temperature sensors, but report very few results and analysis relevant to practical operation of Li-ion cells. In some other studies, details about temperature sensors that may influence results significantly, e.g. size, location, are not provided. The effects of temperature sensors on the cell performance are usually not reported. Commercial cells are used in some studies, with unspecified cell material and internal design.

In this study, 18650-size cylindrical Li-ion cells with multiple micro thermocouples embedded inside their jelly rolls are designed. Experimental cells are manufactured in the Battery Manufacturing Lab at The Pennsylvania State University. Details about temperature sensor size and location, electrode materials, and cell internal structure are described. Temperature distributions along the radial direction of experimental cells are obtained. Effects of various important operating parameters on temperature distribution are investigated, including discharge C rate, ambient temperature, and cooling condition.

*Electrochemical Society Active Member.

^zE-mail: cxw31@psu.edu

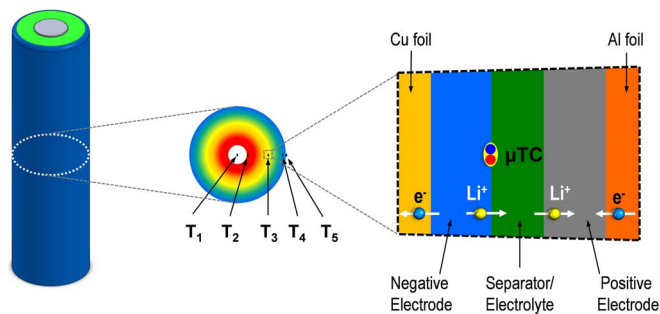


Figure 1. Schematic of an experimental cylindrical Li-ion cell (18650) with embedded micro thermocouples (μ TCs).

Experimental

Design of the experimental Li-ion cell.— Figure 1 shows schematically an experimental 18650 Li-ion cell with multiple micro thermocouples embedded inside its jelly roll, designated as T_2 , T_3 and T_4 along the radial direction. There is also one micro thermocouple embedded in the center of the hollow jelly roll core (white region in the schematic of cross section) which is designated as T_1 . Another thermocouple, designated as T_5 , is attached to the cell surface to monitor the surface temperature for comparison with internal temperatures. The three micro thermocouples in the jelly roll, T_2 , T_3 and T_4 , are equally distributed along the length of the electrode sheets that are wound into the jelly roll during fabrication. All of them are placed between negative electrode and separator as shown in the schematic. T_2 is located at the innermost end of the reaction area and can thus provide the highest local temperature along the radial direction during cell operation. There is no active material or reaction in the hollow jelly roll core, so local temperature, T_1 , is expected to be lower than T_2 .

In this study, T type micro thermocouples (600T, RTD Company, USA) are used for measurement of internal temperatures. Each thermocouple has a wire diameter of $80\ \mu\text{m}$ with an additional $10\ \mu\text{m}$ insulation. The thermocouples are manufactured in such a way that the measuring tip is not thicker than the wire. Slightly smaller thermocouples are available but it is very difficult for them to survive the complicated manufacturing process of a cylindrical cell. The micro thermocouples have no insulation on the measuring tip as received. To prevent their failure in the corrosive electrochemical environment inside the Li-ion cell, a $10\ \mu\text{m}$ layer of parylene is coated on the measuring tip using a special parylene evaporator at Penn State Materials Research Institute Nanofabrication Lab. A conventional T type thermocouple with a diameter of $0.5\ \text{mm}$ (OMEGA Engineering, Inc., USA) is attached to the surface of the experimental cell's stainless steel can to measure surface temperature.

In the experimental cell, $\text{LiNi}_{1/3}\text{Co}_{1/3}\text{Mn}_{1/3}\text{O}_2$ (NCM) and graphite are used as positive and negative electrode materials, respectively. The separator is Celgard 2320 PP/PE/PP trilayer membrane.⁷² The electrolyte is $1.2\ \text{M LiPF}_6$ in EC:EMC:DMC (20:20:60 v%).

To evaluate the influence of embedded micro thermocouples on performance of the experimental cell, a baseline cell is made using identical materials without embedded thermocouples.

Experimental system.— A battery tester (BT2000, Arbin Instruments, USA) is used to control the overall current/voltage of the experimental cell. A multi-channel data acquisition (DAQ) unit (34970A, Agilent Technologies, USA) is used to record the local temperatures in the experimental cell, ambient temperature and cell voltage. All the data reported in this paper is recorded by the DAQ unit with a time interval of one second. To investigate the effect of the ambient temperature on temperature distribution, an environmental chamber (Tenney T10c, Thermal Product Solutions, USA) is used to control the ambient temperature during high- and low-temperature tests. Air is circulated in the chamber to make the temperature field uniform.

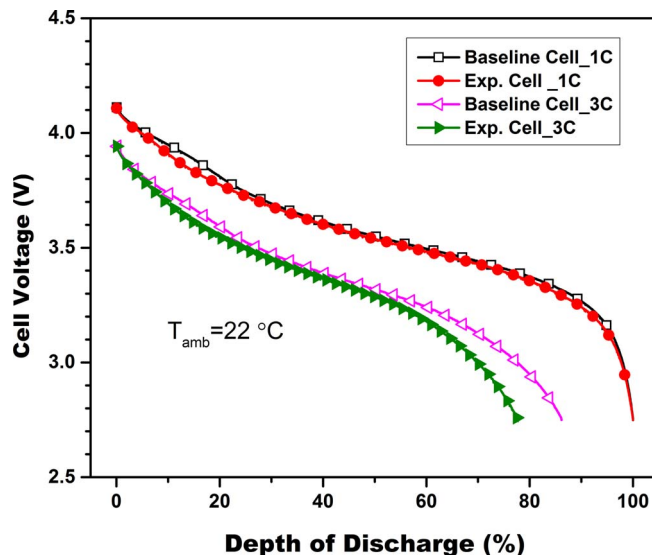


Figure 2. Performance comparison between the baseline and experimental cells.

The air circulation creates a forced convection cooling condition for the experimental cell. The environmental chamber is also used during room temperature tests but without air circulation inside the chamber, eliminating room temperature fluctuations and creating a natural convection cooling condition for the experimental cell. To investigate the effects of cooling condition on the temperature distribution in the experimental cell, a strong forced convection cooling condition is created by a standalone cooling fan blowing directly at the cell.

Test procedures.— Before every test, the battery tester and DAQ unit are turned on and rested for at least one hour, then the cell is fully charged at room temperature ($22 \pm 1^\circ\text{C}$) using a Constant Current-Constant Voltage (CC-CV) protocol ($0.8\ \text{A}$, $4.2\ \text{V max}$, $0.032\ \text{A cutoff}$). Subsequently, the cell is rested for at least one hour (for room temperature tests) or three hours (for tests at other ambient temperatures), allowing open circuit voltage (OCV) and cell temperature to reach equilibrium. For tests under different discharge conditions, the cell is discharged at a specified C rate (based on nominal capacity of $1.6\ \text{Ah}$) until its voltage drops to $2.75\ \text{V}$.

Results and Discussion

Comparison of the baseline cell and the cell with embedded micro thermocouples.— Figure 2 shows the performance comparison between the baseline cell and the experimental cell during 1C and 3C discharge at room temperature. It can be seen that the experimental cell performs very similarly to the baseline cell during all stages of the 1C discharge and most of the 3C discharge. The performance difference increases slightly near the end of the 3C discharge, which can be attributed to higher ohmic resistance at the thermocouple locations. Using smaller micro thermocouples may reduce their influence on cell performance, a subject for future research.

Representative temperature distribution results during 1C discharge.— Figure 3 shows the variation of the local temperatures during 1C discharge and Figure 4 shows the radial distribution of local temperatures at different depths of discharge (DOD). Note that temperature rise is used instead of temperature and DOD is used instead of discharge capacity for convenient comparison between different cases. Dimensionless distance in radial direction, r/r_0 , is used to show locations of the thermocouples. r represents distance of the thermocouples from the center of the cell and r_0 represents the radius of the

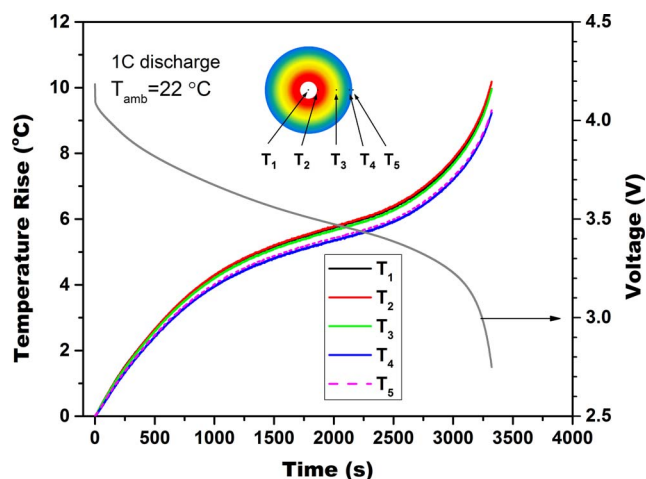


Figure 3. Variation of local temperature rise during a 1C discharge at 22°C.

experimental cell (9.0 mm). To assist understanding of the results, cell voltage is also plotted in Figure 3.

It can be seen from Figure 3 that all the local temperatures increase as discharge proceeds, suggesting that heat generation inside the Li-ion cell during discharge exceeds heat dissipation. Note that the local temperature curves can be roughly divided into three stages. In the beginning stage (0% to ~20% DOD) the temperatures rise very rapidly; in the second stage (~20% to 70% DOD) the temperatures rise more slowly; in the third stage (~70% to 100% DOD) the temperatures rise rapidly again. This behavior can be attributed to the characteristics of heat generation and dissipation in Li-ion cells as revealed by modeling work.^{11,73} In the beginning stage, heat dissipation is trivial due to the small difference between cell surface temperature and ambient temperature, so generated heat is mainly stored in the cell and cause rapid cell temperature rise. As the cell surface temperature grows significantly higher than ambient temperature in the second stage, heat dissipation to the surroundings becomes more significant. In addition, reversible entropic heat generation decreases during this stage.⁷³ Together, these two factors slow down the local temperature rise. As the cell approaches the end of discharge in the third stage, both reversible and irreversible heat generation increase dramatically,^{11,73} causing the cell temperature to rise rapidly again.

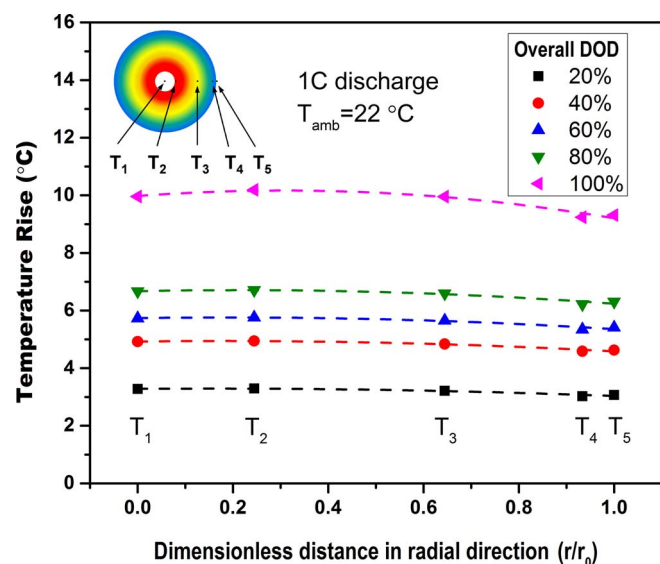


Figure 4. Radial temperature distributions at different DOD levels during a 1C discharge at 22°C.

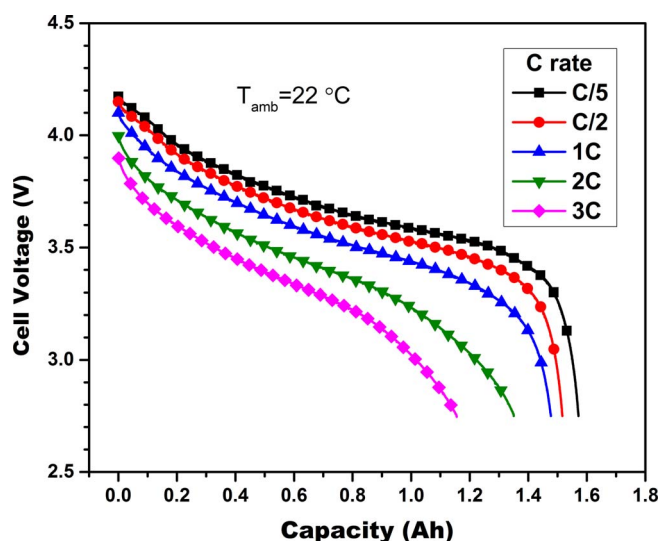


Figure 5. Performance of the experimental cell at various discharge C rates at 22°C.

The spatial temperature distribution results shown in Figure 4 reveal that the temperature gradient along radial direction is quite small during 1C discharge and not observable until the end of discharge. The small temperature gradient along the radial direction can be explained by the thermal behavior of the Li-ion cell. Heat is generated everywhere in the jelly roll during discharge under volumetric heating. Thus the temperature gradient is much smaller than when heat is locally generated in the core and conducted through the jelly roll.

The spatial temperature distribution at the end of 1C discharge is physically reasonable. T_1 is slightly lower than T_2 because there is no reaction in the hollow core of the jelly roll. T_2 is the highest because it is located nearest to the cell center among the thermocouples within the reaction area, consistent with heat transfer from inside the cell to ambient driven by a temperature gradient. The larger temperature gradient near the end of discharge indicates higher heat flux, agreeing with above analysis that heat dissipation to the surroundings is stronger at higher cell temperature.

Effects of C rate on temperature distribution.— C rate is an important parameter for Li-ion battery operation, so temperature distribution in the experimental cell is measured at various C rates (C/5, C/2, 1C, 2C and 3C). Figure 5 shows the discharge performance of the experimental cell at these C rates. Figures 6 and 7 show the variations of local temperatures and temperature distribution at different DOD

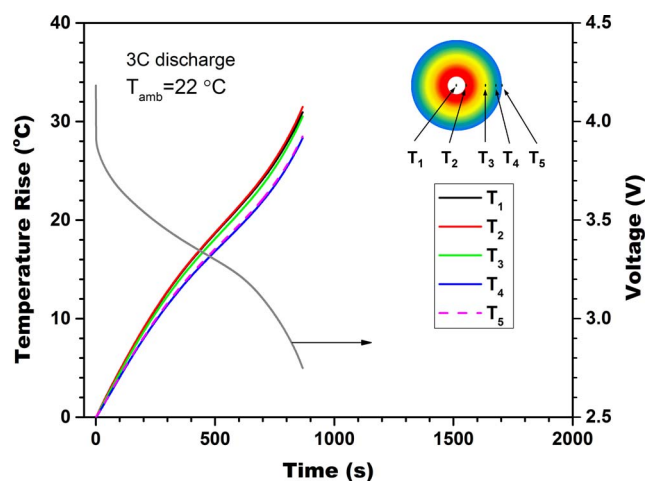


Figure 6. Variation of local temperature rise during a 3C discharge at 22°C.

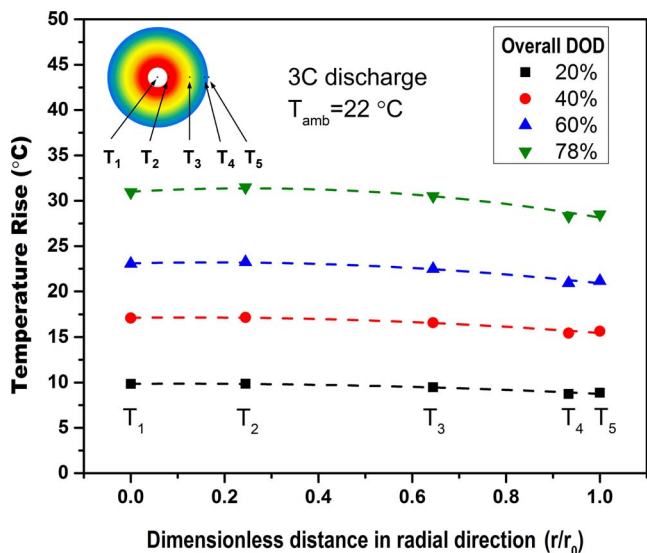


Figure 7. Radial temperature distributions at different DOD during a 3C discharge at 22°C.

levels during 3C discharge, respectively. Figure 8 shows the temperature distributions at the end of discharge in various C rate cases.

It can be seen from Figure 5 that the experimental cell has the typical discharge characteristics of a Li-ion cell, i.e. cell voltage and discharge capacity are lower during higher C rate discharge. The lower voltage and discharge capacity can be attributed to higher overpotential caused by higher local current density.

Comparing Figures 6 and 3, local temperatures increase much higher and faster during higher C rate discharge. For example, T₂ increases roughly 3 times higher and 12 times faster during 3C discharge than during 1C discharge. The huge difference can be attributed to more and faster heat generation during higher C rate discharge. When discharge C rate is higher, local current density is larger and cell overpotential is larger. Both of these lead to more and faster conversion of electrochemical energy to heat according to

$$q = I(U - V_{cell}) - I \left(T \frac{dU}{dT} \right) \quad [1]$$

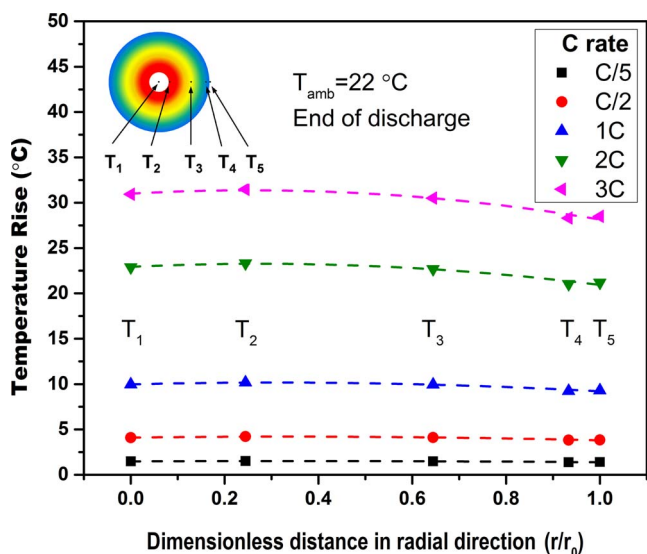


Figure 8. Effects of discharge C rate on the radial temperature distribution at the end of discharge.

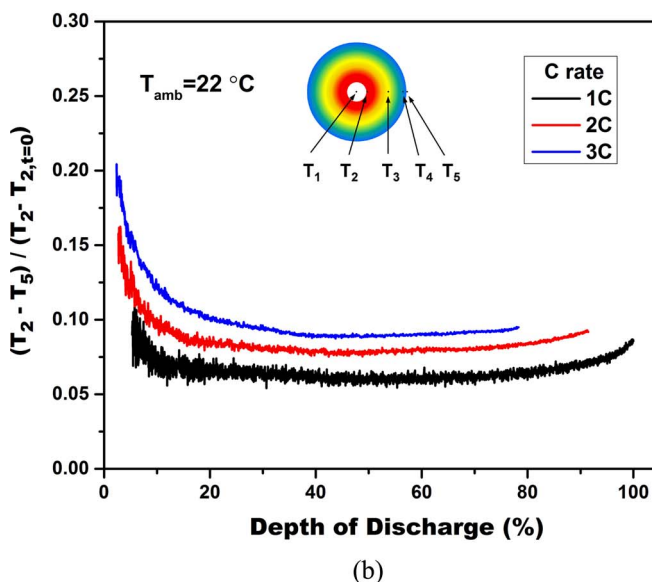
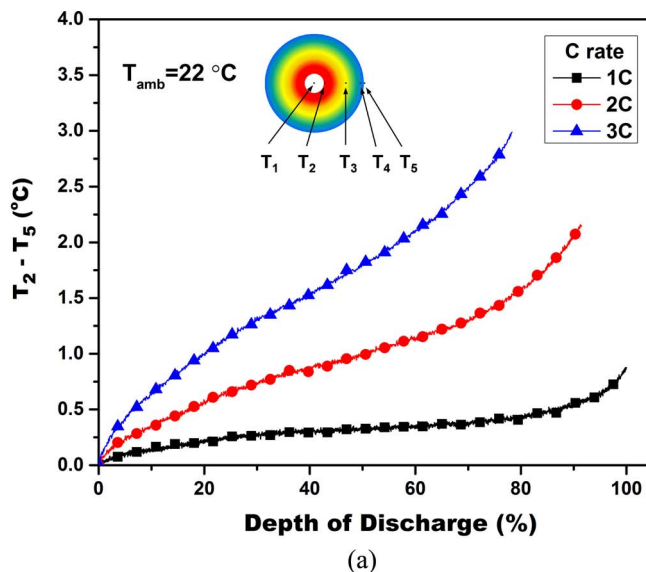


Figure 9. Variation of (a) the temperature gradient and (b) the relative temperature gradient (plotted only when both T₂ and T₅ increase more than 1°C) during discharge at different C rates.

where q is heat generation rate, I is current, U is open circuit voltage, V_{cell} is cell voltage, and T is temperature (K). The term $I(U - V_{cell})$ represents irreversible heat generation and $I(T \frac{dU}{dT})$ represents reversible heat generation.

Comparison between Figures 7 and 4 shows that the temperature distribution patterns during 3C and 1C discharge are quite similar. T₂ is the highest among the five local temperatures and the temperature gradient is quite small in comparison with the temperature rise.

Figure 8 shows a higher temperature rise and a larger temperature gradient during higher C rate discharge. This agrees with the above analysis that heat is generated more and faster during higher C rate discharge, leading to higher temperature rise. The higher temperature rise then results in more heat dissipation from the cell to the ambient and a larger temperature gradient inside the cell to drive heat transfer from inside to surface.

A similar pattern of temperature distribution at different DOD and in different C rate cases inspires an examination of the relative temperature gradient during discharge. Figure 9 shows the variation of temperature gradient and the relative temperature gradient during

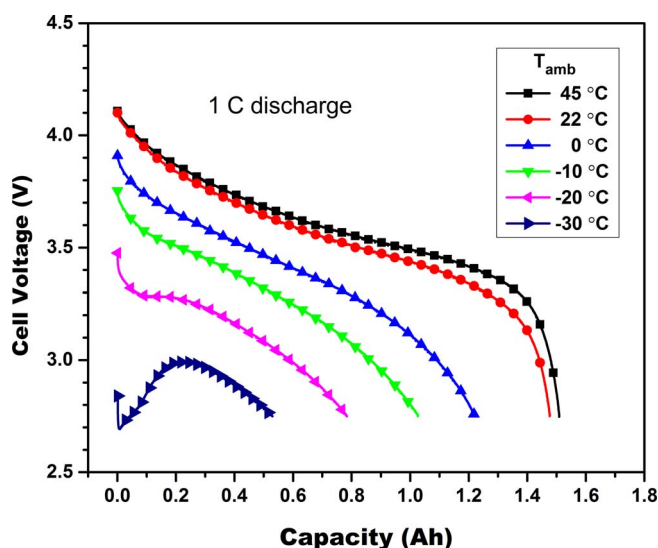


Figure 10. Performance of the experimental cell at various ambient temperatures.

1C, 2C and 3C discharge. Here, the temperature gradient is defined as the difference between T_2 and T_5 , the highest temperature and the lowest temperature in the radial direction, respectively. The relative temperature gradient is defined as the difference between T_2 and T_5 divided by the increase of T_2 . To reduce the effects of large error due to small temperature rise at the beginning of discharge, the relative temperature gradient is plotted only after both T_2 and T_5 increase more than 1°C in Figure 9. While the temperature gradient increases in a trend similar to that of local temperatures, the relative temperature gradient behaves very differently. It decreases quickly at the beginning of discharge but then enters an almost flat region and remains stable almost to the end of discharge. Note that the relative temperature gradient is quite small, <0.1 , in the flat region. This indicates that the assumption of uniform temperature distribution in some battery models is reasonable in such regions. Higher relative temperature gradient in the initial region indicates greater difference between the internal temperature and surface temperature.

Effects of ambient temperature on the temperature distribution.—Ambient temperature is another important operating parameter for Li-ion batteries, especially for automotive Li-ion batteries that need to operate over a wide range of temperatures. In this study, the experimental cell is tested at various temperatures of practical interest (45°C , 25°C , 0°C , -10°C , -20°C , and -30°C) to investigate the effects on temperature distribution. Figure 10 shows the 1C discharge performance of the experimental cell at various ambient temperatures. Figures 11 and 12 show the variation and radial distribution of local temperatures during -30°C discharge for comparison with discharge at room temperature. Figure 13 shows the radial distribution of local temperatures at the end of discharge at various ambient temperatures. Note that the cell cutoff voltage during -30°C discharge is allowed to be temporarily lower than 2.75 V due to the very low performance at such low temperature.

It can be seen from Figure 10 that the performance of the experimental cell at low temperatures is significantly lower than that at room temperature, while performance at 45°C is only slightly better. This can be attributed to the much higher internal resistance of a Li-ion cell at low temperature according to previous studies.⁷ It is interesting to note that at very low temperatures, e.g., -30°C , the cell voltage initially decreases sharply but then increases dramatically before decreasing again. The initial sharp decrease of cell voltage can be attributed to very high internal resistance of the Li-ion cell at low temperature. Higher resistance leads to faster irreversible heat generation, so the cell temperature increases rapidly, as shown in

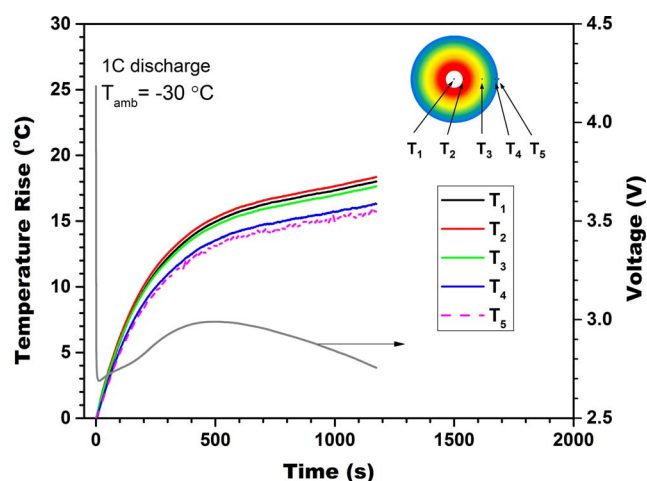


Figure 11. Variation of local temperature rise during a 1C discharge at -30°C .

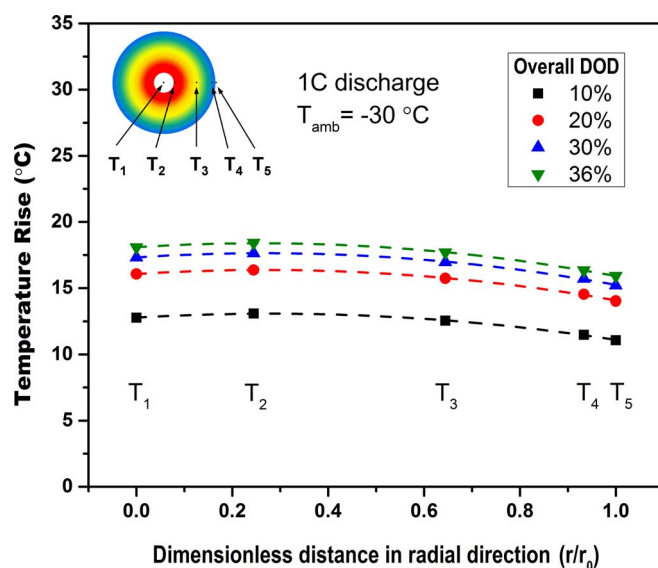


Figure 12. Radial temperature distributions at different DOD during a 1C discharge at -30°C .

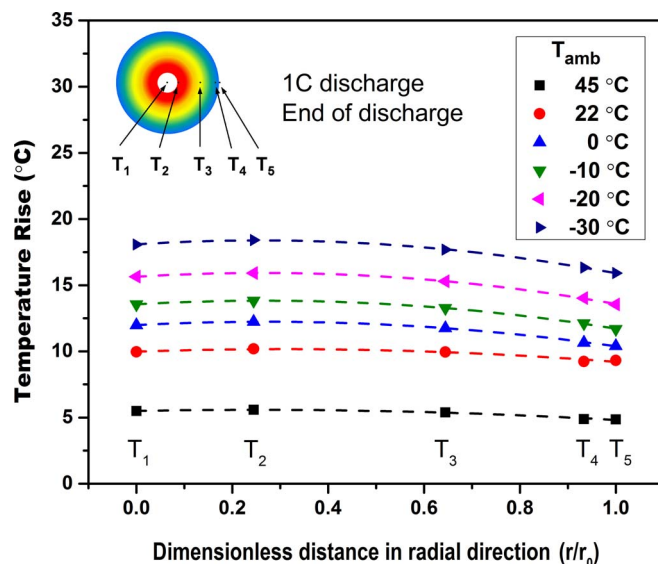


Figure 13. Effects of ambient temperature on the radial temperature distribution at the end of discharge.

Figure 11. Internal temperatures increase 10°C within 200 seconds, leading to dramatically lower internal resistance of the experimental cell and thus rapid rise of cell voltage. With the recovery of the cell voltage, heat generation slows down and then decreased SOC begins to play a more important role, causing cell voltage to decrease as in the other cases.

The dramatic effects of internal temperature on the low temperature performance of the Li-ion battery suggest that tremendous heat generation can be very useful for efficient operation of Li-ion batteries at low temperature with proper thermal management strategies. Some strategies have been explored very recently by Ji and Wang⁴² using an electrochemical-thermal coupled model. To make the best use of heat generation at low temperature, which drains precious electric energy storage, it is important to use internal temperature as an input of the thermal management controller considering that internal temperature is a better indicator of internal state than surface temperature.

Comparison of Figures 11 and 12 with Figures 3 and 4 shows that local temperatures increase higher and faster at lower ambient temperature. The temperature gradient is also obviously larger. However, the temperature gradient pattern is similar. Figure 13 shows more clearly that the temperature distribution pattern is very similar at different ambient temperatures. Note that the more temperature distribution at 22°C can be attributed to a different cooling condition in this case. As mentioned previously, the tests at other ambient temperatures are done in the environmental chamber with air circulation in the chamber. But the test at 22°C has no air circulation in the chamber.

The effects of ambient temperature on temperature gradient and relative temperature gradient are also explored, as shown in Figure 14. The temperature gradient increases more and much faster at lower ambient temperature, especially at the beginning of discharge when the cell internal temperature and resistance are lowest. The relative temperature gradient in different cases also shows a pattern of initially decreasing and then entering a flat region. The relative temperature gradient curves almost overlap in cases of subzero temperatures in which cooling conditions are same. It suggests the dependence of relative temperature gradient on cooling conditions.

Effects of cooling condition on the temperature distribution.— Due to the detrimental effects of high temperature on durability and safety, Li-ion batteries typically need to be cooled to prevent overheating. In addition, the relative temperature gradient results indicate a dependence on cooling conditions. Therefore, the effects of cooling on temperature distribution are investigated in this study. Two cases are investigated. The first case involves testing the experimental cell with natural convection cooling by placing the cell in environmental chamber without air circulation. The second case involves testing the cell with forced convection cooling using a fan.

Figure 15 shows the effects of cooling conditions on cell performance during 3C discharge. It can be seen from Figure 15 that the performance with a cooling fan is initially similar to that without a cooling fan, but decreases substantially in the later part of discharge and the discharge capacity is significantly reduced. This can be attributed to the much slower cell temperature rise with stronger cooling. The experimental cell has same initial temperature in both cases, so the initial performances are very similar. Then, with the considerable heat generation during 3C discharge, the cell internal temperature begins to rise quickly. Stronger cooling enhances heat dissipation, and thus leads to slower rise of cell temperatures, especially local temperatures near and on the surface. Figure 16 shows the variation of local temperatures during 3C discharge with a cooling fan. Comparing Figures 16 and 6, the local temperatures with a cooling fan increase only about half of those without a cooling fan by the end of discharge. Lower temperature suggests higher cell internal resistance, and therefore lower performance and discharge capacity.

Figure 17 shows the spatial temperature distribution during 3C discharge with cooling fan. It can be seen that there is a large temperature gradient along the radial direction, especially near the cell surface. The temperature gradient also becomes larger at higher DOD levels. Comparison with Figure 7 shows that local temperature rise and

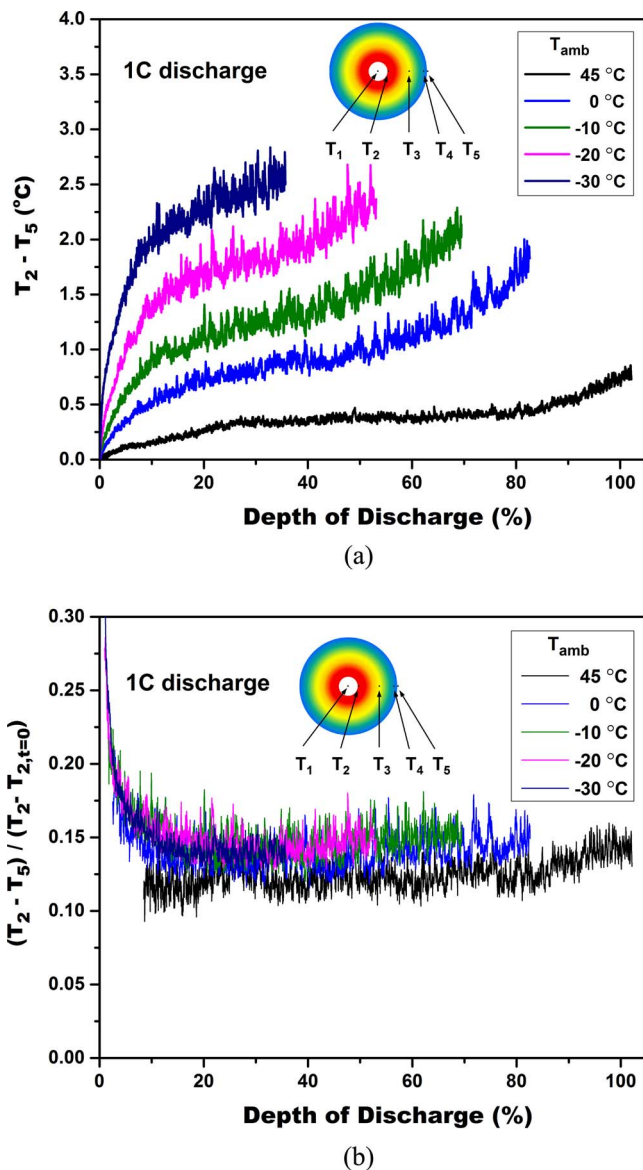


Figure 14. Variation of (a) the temperature gradient and (b) the relative temperature gradient (plotted only when both T_2 and T_5 increase more than 1°C) during discharge at various ambient temperatures.

spatial temperature gradient are smaller than those without a cooling fan at the same DOD levels.

Figure 18 compares the variation of the temperature gradient and relative temperature gradient during 3C discharge under the two different cooling conditions. It can be seen that both the temperature gradient and the relative temperature gradient are much larger with stronger cooling. Note that the relative temperature gradient with a cooling fan is about 3 times larger than that during natural convection cooling, reaching a value of 0.3. This suggests conflicting effects of strong cooling from outside of the Li-ion cell. While strong cooling can effectively prevent overheating of Li-ion cells, it can cause a large temperature gradient. Considering the fact that local performance depends significantly on local temperature, the non-uniform current distribution in large format Li-ion battery cells³³⁻³⁵ may be exacerbated by such larger temperature gradient.

Correlation between the relative temperature gradient and cooling coefficient.— The above results indicate a correlation between relative temperature gradient and cooling condition. To investigate their

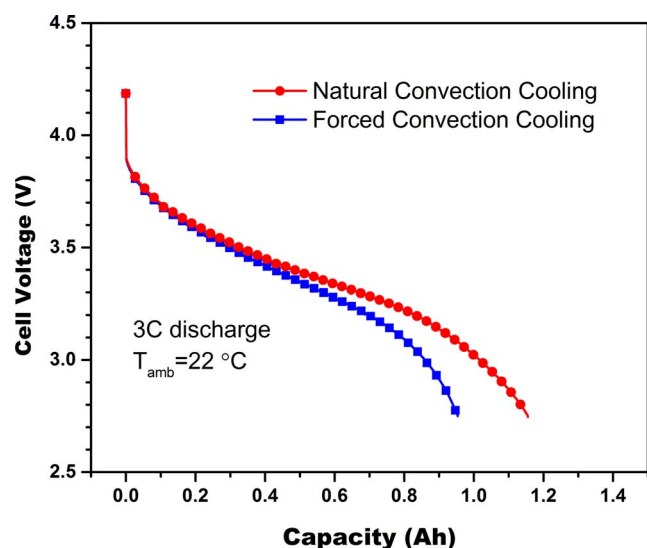
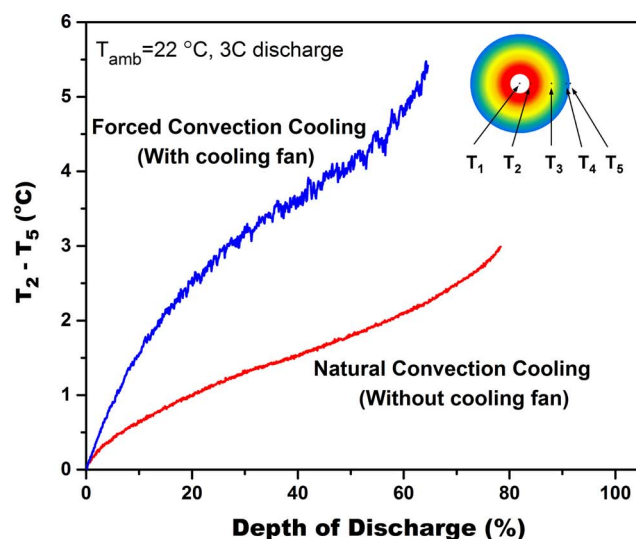


Figure 15. Performance of the experimental cell with natural and forced convection cooling.



(a)

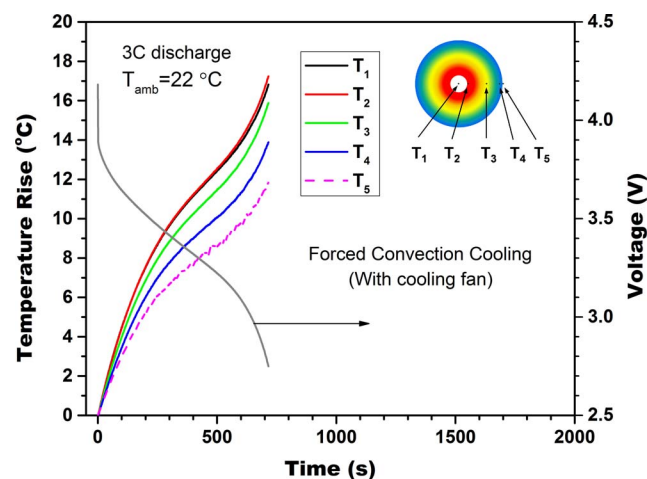
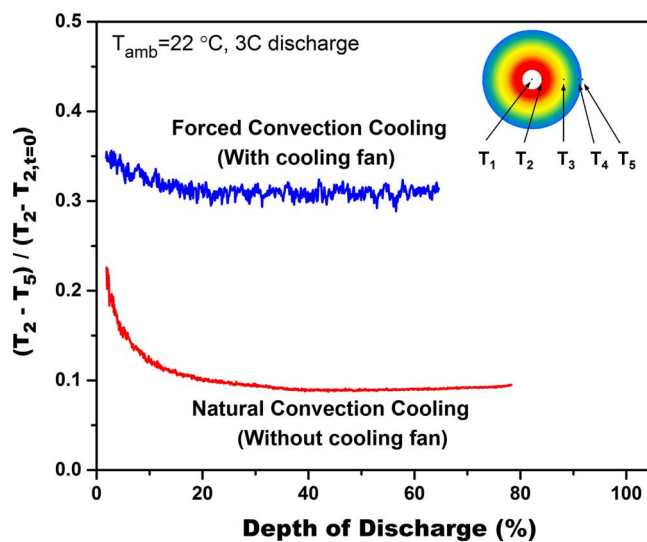


Figure 16. Variation of local temperature rise during a 3C discharge at 22°C with forced convection cooling.



(b)

Figure 18. Variation of (a) the temperature gradient and (b) the relative temperature gradient (plotted only when both T_2 and T_5 increase more than 1°C) during 3C discharge under different cooling conditions.

correlation quantitatively, the cooling coefficient is estimated using a method similar to a previous work by Ji and Wang.¹¹ Then, the average relative temperature gradient (from 30% DOD to end of discharge), which is used to represent the value during the flat region, is correlated with the estimated cooling coefficient.

To estimate the cooling coefficient, the characteristic cooling time needs to be firstly estimated by plotting the surface temperature rise in log scale versus time after discharge and then fitting the curves according to

$$T_5 - T_{amb} = (T_{5,i} - T_{amb}) \times \exp\left(\frac{-t}{\tau}\right) \quad [2]$$

where τ is the characteristic cooling time, $T_{5,i}$ is initial temperature of T_5 . Then curve fittings are performed in the time range of 100 s to 600 s, following similar practice in the previous work,¹¹ to avoid the mixing effect right after discharge and larger error at later times due to smaller temperature difference.

Figure 19 shows representative results of estimated characteristic cooling time, which is then used to estimate cooling coefficient

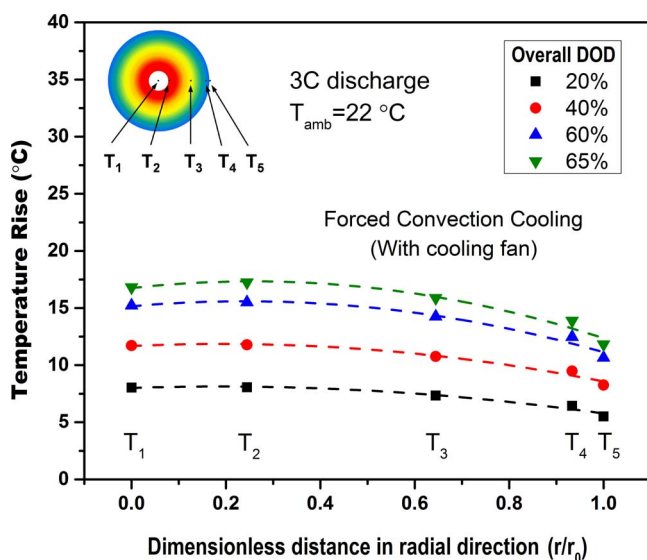


Figure 17. Radial temperature distributions at different DOD during a 3C discharge at 22°C with forced convection cooling.

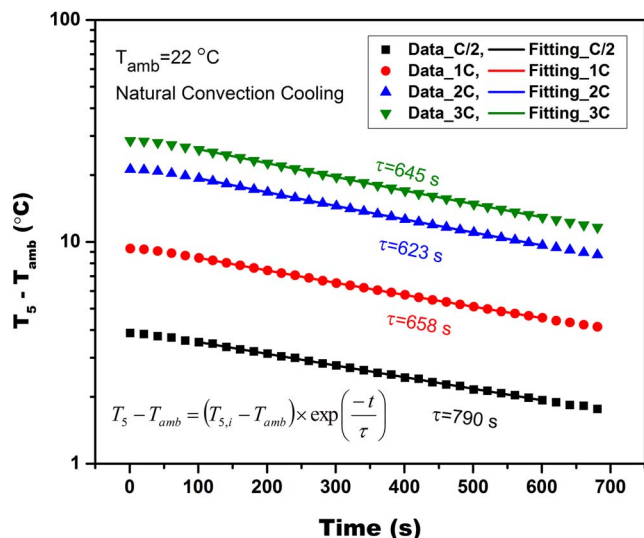


Figure 19. Variation of the cell surface temperature for estimation of surface convection heat transfer coefficient.

according to:

$$h = \frac{mc_p}{\tau A_s} \quad [3]$$

where h is the cooling coefficient, m is mass of experimental cell (41 gram in this study), c_p is the specific heat of experimental cell (assumed to be $823 \text{ J kg}^{-1} \text{ K}^{-1}$),^{11,74} and A_s is the cell surface area ($\sim 0.00419 \text{ m}^2$).¹¹

Cooling coefficients in other cases are also estimated using the same method. The estimated cooling coefficients in various cases are then correlated with the relative temperature gradients as plotted in Figure 20. Note that the data points labeled as “Natural Convection” refer to the cases of various C rate (C/2, 1C, 2C and 3C) under natural convection conditions. Those labeled as “Forced Convection (circulation fan in environmental chamber)” refer to the cases of different ambient temperature (45°C , 25°C , 0°C , -10°C , and -20°C). Data at -30°C were not enough for accurate estimation, thus not used). The data point labeled as “Forced Convection (standalone cooling fan)” refers to the case of 3C discharge with the experimental cell cooled by a standalone cooling fan. It can be seen that the relative temperature

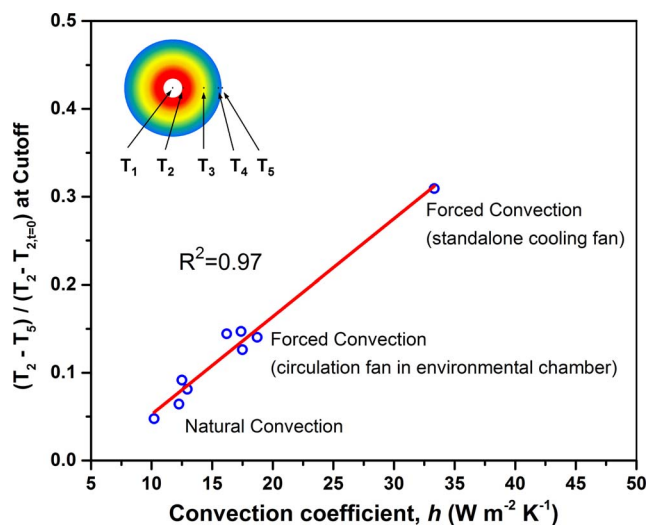


Figure 20. Correlation between the relative temperature gradient and convection heat transfer coefficient.

gradient increases almost linearly with cooling coefficient during the testing range. The correlation suggests that it is reasonable to assume a uniform temperature distribution in the experimental cell with natural convection cooling when the relative temperature gradient is small. But the relative temperature gradient becomes large with strong forced convection cooling, making the assumption of uniform temperature distribution not applicable.

Conclusions

Temperature is critical to the performance, durability and safety of Li-ion batteries. To investigate the thermal behavior of the Li-ion battery and provide valuable experimental data for validation of electrochemical-thermal coupled (ECT) battery models, 18650-size cylindrical cells with multiple embedded micro thermocouples are designed and manufactured. Temperature distribution along the radial direction in an experimental cell under various C rate, ambient temperature and cooling conditions are obtained. It is found that the temperature gradient is larger at higher C rates and lower ambient temperatures because more heat is generated under such conditions. Stronger cooling results in lower temperature rise but larger temperature gradient due to increased heat dissipation from the cell surface to the surroundings. Relative temperature gradient during discharge is initially large, but gradually decreases and then remains almost constant until the end of discharge. Correlation between relative temperature gradient and cooling coefficient suggests that the assumption of uniform temperature distribution is applicable under natural cooling conditions but not applicable under strong forced convection cooling conditions. With the details of experimental cell design reported, the results provide valuable experimental data that can be readily used for validation. Further studies under transient and extreme conditions are warranted.

Acknowledgments

The authors gratefully acknowledge funding from The United States Department of Energy (CAEBAT Program) through a subcontract from EC Power. The authors are thankful to Dr. Yan Ji from ECEC for valuable discussions and Dr. Bangzhi Liu from Materials Research Institute for help in parylene coating of micro thermocouples. This work was also partially supported by the Pennsylvania State University Materials Research Institute Nanofabrication Lab and the National Science Foundation Cooperative Agreement No. ECS-0335765.

References

- C. D. Rahn and C. Y. Wang, *Battery Systems Engineering*, John Wiley & Sons Ltd (2013).
- D. Doughty and E. P. Roth, *The Electrochemical Society Interface*, **Summer**, 37 (2012).
- DOE, Fiscal Year 2012 Progress Report for Energy Storage R&D, DOE/EE-0844, <http://energy.gov/eere/vehicles/fy-2012-progress-report-energy-storage-rd>, (2013), accessed on April 28th, 2014.
- J. B. Goodenough and Y. Kim, *Chemistry of Materials*, **22**, 587 (2010).
- T. M. Bandhauer, S. Garimella, and T. F. Fuller, *Journal of The Electrochemical Society*, **158**, R1 (2011).
- S. S. Zhang, K. Xu, and T. R. Jow, *Journal of Power Sources*, **115**, 137 (2003).
- S. S. Zhang, K. Xu, and T. R. Jow, *Electrochimica Acta*, **49**, 1057 (2004).
- Y. Zhang and C. Y. Wang, *Journal of The Electrochemical Society*, **156**, A527 (2009).
- D. P. Abraham, J. R. Heaton, S. H. Kang, D. W. Dees, and A. N. Jansen, *Journal of The Electrochemical Society*, **155**, A41 (2008).
- Y. Zhang, C. Y. Wang, and X. Tang, *Journal of Power Sources*, **196**, 1513 (2011).
- Y. Ji, Y. Zhang, and C. Y. Wang, *Journal of The Electrochemical Society*, **160**, A636 (2013).
- H.-p. Lin, D. Chua, M. Salomon, H.-C. Shiao, M. Hendrickson, E. Plichta, and S. Slane, *Electrochemical and Solid-State Letters*, **4**, A71 (2001).
- J. Fan and S. Tan, *Journal of The Electrochemical Society*, **153**, A1081 (2006).
- M. C. Smart and B. V. Ratnakumar, *Journal of The Electrochemical Society*, **158**, A379 (2011).
- M. Broussely, S. Herreyre, P. Biensan, P. Kasztejna, K. Nechev, and R. J. Staniewicz, *Journal of Power Sources*, **97-98**, 13 (2001).
- E. V. Thomas, H. L. Case, D. H. Doughty, R. G. Jungst, G. Nagasubramanian, and E. P. Roth, *Journal of Power Sources*, **124**, 254 (2003).

17. J. Vetter, P. Novák, M. R. Wagner, C. Veit, K. C. Möller, J. O. Besenhard, M. Winter, M. Wohlfahrt-Mehrens, C. Vogler, and A. Hammouche, *Journal of Power Sources*, **147**, 269 (2005).
18. S. Santhanagopalan, Q. Zhang, K. Kumaresan, and R. E. White, *Journal of the Electrochemical Society*, **155**, A345 (2008).
19. E. V. Thomas, I. Bloom, J. P. Christophersen, and V. S. Battaglia, *Journal of Power Sources*, **184**, 312 (2008).
20. H. Maleki, G. Deng, A. Anani, and J. Howard, *Journal of The Electrochemical Society*, **146**, 3224 (1999).
21. M. N. Richard and J. R. Dahn, *Journal of The Electrochemical Society*, **146**, 2068 (1999).
22. A. Hammami, N. Raymond, and M. Armand, *Nature*, **424**, 635 (2003).
23. C. L. Campion, W. Li, W. B. Euler, B. L. Lucht, B. Ravdel, J. F. DiCarlo, R. Gitzendanner, and K. M. Abraham, *Electrochemical and Solid-State Letters*, **7**, A194 (2004).
24. C. L. Campion, W. Li, and B. L. Lucht, *Journal of the Electrochemical Society*, **152**, A2327 (2005).
25. E. P. Roth and C. J. Orendorff, *The Electrochemical Society Interface*, **Summer**, 45 (2012).
26. E. P. Roth and D. H. Doughty, *Journal of Power Sources*, **128**, 308 (2004).
27. C. Y. Jhu, Y. W. Wang, C. M. Shu, J. C. Chang, and H. C. Wu, *Journal of Hazardous Materials*, **192**, 99 (2011).
28. J. B. Robinson, J. A. Darr, D. S. Eastwood, G. Hinds, P. D. Lee, P. R. Shearing, O. O. Taiwo, and D. J. L. Brett, *Journal of Power Sources*, **252**, 51 (2014).
29. X. Feng, M. Fang, X. He, M. Ouyang, L. Lu, H. Wang, and M. Zhang, *Journal of Power Sources*, **255**, 294 (2014).
30. H. Maleki, S. A. Hallaj, J. R. Selman, R. B. Dinwiddie, and H. Wang, *Journal of The Electrochemical Society*, **146**, 947 (1999).
31. S. C. Chen, C. C. Wan, and Y. Y. Wang, *Journal of Power Sources*, **140**, 111 (2005).
32. S. C. Chen, Y. Y. Wang, and C. C. Wan, *Journal of The Electrochemical Society*, **153**, A637 (2006).
33. G. Zhang, C. E. Shaffer, C. Y. Wang, and C. D. Rahn, *Journal of the Electrochemical Society*, **160**, A2299 (2013).
34. G. Zhang, C. E. Shaffer, C. Y. Wang, and C. D. Rahn, *Journal of The Electrochemical Society*, **160**, A610 (2013).
35. W. Zhao, G. Luo, and C. Y. Wang, *Journal of Power Sources*, **257**, 70 (2014).
36. M. Doyle, T. F. Fuller, and J. Newman, *Journal of The Electrochemical Society*, **140**, 1526 (1993).
37. W. B. Gu and C. Y. Wang, in *Lithium Batteries. Proceedings of the International Symposium, 17-22 Oct. 1999*, p. 748, Lithium Batteries. Proceedings of the International Symposium (Electrochemical Society Proceedings Vol.99-25), Pennington, NJ, USA (2000).
38. K. Smith and C. Y. Wang, *Journal of Power Sources*, **160**, 662 (2006).
39. S. Santhanagopalan, Q. Guo, P. Ramadass, and R. E. White, *Journal of Power Sources*, **156**, 620 (2006).
40. V. Ramadesigan, P. W. C. Northrop, S. De, S. Santhanagopalan, R. D. Braatz, and V. R. Subramanian, *Journal of The Electrochemical Society*, **159**, R31 (2012).
41. W. Fang, O. J. Kwon, and C.-Y. Wang, *International Journal of Energy Research*, **34**, 107 (2010).
42. Y. Ji and C. Y. Wang, *Electrochimica Acta*, **107**, 664 (2013).
43. M. Guo, G. Sikha, and R. E. White, *Journal of The Electrochemical Society*, **158**, A122 (2011).
44. C. Y. Wang and V. Srinivasan, *Journal of Power Sources*, **110**, 364 (2002).
45. V. Srinivasan and C. Y. Wang, *Journal of The Electrochemical Society*, **150**, A98 (2003).
46. G. Luo and C. Y. Wang, in *Lithium-Ion Batteries: Advanced Materials and Technologies*, X. Yuan, H. Liu, and J. Zhang Editors, CRC Press (2012).
47. W. Zhao and C. Y. Wang, *221st ECS Meeting*, **MA2012-01**, 536 (2012).
48. Y. Inui, Y. Kobayashi, Y. Watanabe, Y. Watase, and Y. Kitamura, *Energy Conversion and Management*, **48**, 2103 (2007).
49. G. H. Kim, A. Pesaran, and R. Spotnitz, *Journal of Power Sources*, **170**, 476 (2007).
50. S. Santhanagopalan, P. Ramadass, and J. Zhang, *Journal of Power Sources*, **194**, 550 (2009).
51. K.-J. Lee, G.-H. Kim, and K. Smith, *218th ECS Meeting*, **MA2010-02**, 1114 (2010).
52. M. Fleckenstein, O. Bohlen, M. A. Roscher, and B. Baker, *Journal of Power Sources*, **196**, 4769 (2011).
53. D. H. Jeon and S. M. Baek, *Energy Conversion and Management*, **52**, 2973 (2011).
54. X. Zhang, *Electrochimica Acta*, **56**, 1246 (2011).
55. K.-J. Lee, K. Smith, A. Pesaran, and G.-H. Kim, *Journal of Power Sources*, **241**, 20 (2013).
56. M. Guo and R. E. White, *Journal of Power Sources*, **221**, 334 (2013).
57. P. Taheri and M. Bahrami, *SAE International Journal of Passenger Cars- Electronic and Electrical Systems*, **5**, 164 (2012).
58. R. A. Leising, M. J. Palazzo, E. S. Takeuchi, and K. J. Takeuchi, *Journal of the Electrochemical Society*, **148**, A838 (2001).
59. R. A. Leising, M. J. Palazzo, E. S. Takeuchi, and K. J. Takeuchi, *Journal of Power Sources*, **97-98**, 681 (2001).
60. Y. Zeng, K. Wu, D. Wang, Z. Wang, and L. Chen, *Journal of Power Sources*, **160**, 1302 (2006).
61. T. D. Hatchard, S. Trussler, and J. R. Dahn, *Journal of Power Sources*, **247**, 821 (2014).
62. K. Onda, H. Kameyama, T. Hanamoto, and K. Ito, *Journal of the Electrochemical Society*, **150**, A285 (2003).
63. K. Onda, T. Ohshima, M. Nakayama, K. Fukuda, and T. Araki, *Journal of Power Sources*, **158**, 535 (2006).
64. C. Forgez, D. Vinh Do, G. Friedrich, M. Morcrette, and C. Delacourt, *Journal of Power Sources*, **195**, 2961 (2010).
65. C. Y. Lee, S. J. Lee, C. T. Hsieh, M. S. Tang, J. Y. Lin, Y. M. Lo, P. C. Chen, D. Y. Chang, and R. S. Juang, *Proceedings of the 6th IEEE International Conference on Nano/Micro Engineered and Molecular Systems*, Kaohsiung, Taiwan, February 20-23 (2011).
66. C. Y. Lee, S. J. Lee, M. S. Tang, and P. C. Chen, *Sensors*, **11**, 9942 (2011).
67. C. Y. Lee, S. J. Lee, Y. H. Chen, M. Y. Chung, K. C. Han, Y. M. Chang, and M. S. Tang, *International Journal of Electrochemical Science*, **8**, 2968 (2013).
68. R. Srinivasan, B. G. Carkhuff, M. H. Butler, and A. C. Baisden, *Electrochimica Acta*, **56**, 6198 (2011).
69. R. Srinivasan, B. G. Carkhuff, M. H. Butler, A. C. Baisden, and O. M. Uy, in *Energy Harvesting and Storage: Materials, Devices, and Applications II, April 25-28, 2011*, The Society of Photo, Proceedings of SPIE - The International Society for Optical Engineering, Orlando, FL, United states (2011).
70. J. P. Schmidt, S. Arnold, A. Loges, D. Werner, T. Wetzler, and E. Ivers-Tiffée, *Journal of Power Sources*, **243**, 110 (2013).
71. Z. Li, J. Zhang, B. Wu, J. Huang, Z. Nie, Y. Sun, F. An, and N. Wu, *Journal of Power Sources*, **241**, 536 (2013).
72. Celgard, Celgard High Performance Battery Separators, http://www.celgard.com/pdf/library/Celgard_Product_Comparison_10002.pdf (2009), accessed on April 8th, 2014.
73. W. Lu, I. Belharouak, D. Vissers, and K. Amine, *Journal of The Electrochemical Society*, **153**, A2147 (2006).
74. E. P. Roth, Thermal Abuse Performance of MOLI, Panasonic and Sanyo 18650 Li-Ion Cells, *SANDIA REPORT*, SAND2004-6721 (2005).